Resonant dampers for parametric instabilities in gravitational wave detectors

S. Gras, P. Fritschel, L. Barsotti, and M. Evans

Phys. Rev. D **92**, 082001 — Published 2 October 2015

DOI: 10.1103/PhysRevD.92.082001

Resonant Dampers for Parametric Instabilities in Gravitational Wave Detectors

S. Gras,* P. Fritschel, L. Barsotti, and M. Evans
Massachusetts Institute of Technology, 185 Albany St. NW22-295, 02139 MA, USA

Advanced gravitational wave interferometric detectors will operate at their design sensitivity with nearly ∼1MW of laser power stored in the arm cavities. Such large power may lead to the uncontrolled growth of acoustic modes in the test masses due to the transfer of optical energy to the mechanical modes of the arm cavity mirrors. These parametric instabilities have the potential of significantly compromising the detector performance and control. Here we present the design of "acoustic mode dampers" that use the piezoelectric effect to reduce the coupling of optical to mechanical energy. Experimental measurements carried on an Advanced LIGO-like test mass have shown a 10-fold reduction in the amplitude of several mechanical modes, thus suggesting that this technique can greatly mitigate the impact of parametric instabilities in advanced detectors.

PACS numbers: 04.80.Nn, 07.60.Ly, 77.84.Cg, 85.50.-n
Keywords: gravitational wave detector; paramteric instabilities; resonant damper; piezoelectric effect

I. INTRODUCTION

The network of advanced gravitational wave detectors currently under construction (two LIGO [1] detectors in the USA, the Advanced Virgo [2] detector in Italy, and Kagra [3] in Japan) promises to open the new window of gravitational wave astronomy within this decade. These large optical interferometers are built to make extremely high precision measurement of the test mass motion induced by gravitational waves [4].

Sensitivity to gravitational wave strains of order 10^{-24} requires high optical power circulating in the arm cavities of these detectors. For instance, up to 750 kW of optical power will be sustained in the steady-state regime inside the Advanced LIGO arm cavities.

It has been experimentally observed that the stored energy in a resonant cavity can leak from the optical modes to the mechanical modes of the cavity mirrors via a 3-mode interaction [5]. Given sufficiently high circulating optical power, and mirror materials with very low mechanical loss as required to avoid thermal noise, the uncontrolled growth of test mass acoustic modes can lead to Parametric Instabilities (PI) [6, 7]. If left unaddressed, PI will prevent high power operation, and thus limit the astrophysical output of gravitational wave detectors. While Advanced LIGO will serve as the primary example in this paper, all advanced gravitational wave detectors are susceptible to these instabilities.

Several schemes have been proposed to damp PI [8, 9]. In particular, solutions directly applicable to Advanced LIGO involve active damping of acoustic modes by means of the test mass electro-static drive actuators [10], and thermal tuning of the optical modes using the test mass ring heaters [11]. A significant constraint on any technique is that it must preserve the inherently low mechanical loss of the test mass in the gravitational wave frequency band to maintain a low level of thermal noise.

Here we present a novel method to passively control PI by reducing the Q-factor of the test mass acoustic modes with small resonant dampers. These "acoustic mode dampers" (AMD) dissipate the strain energy of the test mass mode through a resistive element after converting it to electrical energy via the piezoelectric effect (see figure 2).

The resonant nature of the AMD allows it to effectively damp test mass acoustic modes without introducing significant mechanical loss at lower frequencies where thermal noise can limit detector performance. With respect to other proposed solutions, this approach has the advantage of being simple, self-contained, and completely passive. Models indicate that AMDs can provide a broadband reduction in the Q of mechanical modes relevant to PI, and are therefore particularly beneficial in the presence of a large number of unstable modes.

The structure of this paper is as follows. In section II we set the stage by giving a brief overview of parametric instabilities, including equations of particular relevance to evaluating AMD performance. section III presents a simple 1-dimensional model of the AMD which highlights the principles of AMD operation. This is followed by a description of the detailed finite element model (FEM) used to analyze the AMDs ability to suppress PI when attached to an Advanced LIGO test mass. The FEM predictions are compared with experimental results from a full-scale prototype in section IV. Finally, in section V we discuss an AMD design that will provide Advanced LIGO with protection from instabilities, without significantly increasing test mass thermal noise.

II. PARAMETRIC INSTABILITIES (PI)

The acousto-optic interactions responsible for parametric instabilities have been extensively studied [6, 8, 12]. They consist of a scattering process and radiation pressure operating together in an optical cavity in a closed-loop manner. The graphical representation of this process is shown in figure 1.

* E-mail me at: sgras@ligo.mit.edu

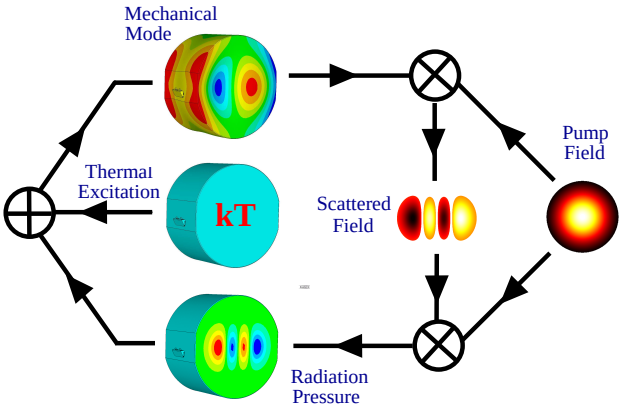

FIG. 1. PI described as a positive feedback process. The process is started when thermally perturbed mirror surface distorts a steady state cavity field inside the interferometer arm cavity. Two transverse optical sidebands are created. Both sidebands exert force on the test mass via radiation pressure. When the energy dissipation of the acoustic mode and the rate of work done by the radiation pressure are unbalanced, one of the sidebands excites the exponential growth of the acoustic mode amplitude. The dynamic of this process is commonly described in terms of the parametric gain R, with $R > 1$ in the case of instability.

The e-folding growth time, or "ring-up time", of an acoustic mode in the presence of a 3-mode interaction is $\tau = 2Q_m/(\omega_m(R-1))$ [13], where Q_m and ω_m are the Q-factor and angular frequency of the mode, respectively, and R is the parametric gain. When $R > 1$ the amplitude increases exponentially until a saturation point is reached [14]. The parametric gain R for the single opto-mechanical interaction can be approximated as

$$R \approx P_c \Lambda Q_m \Gamma(\delta\nu_{hom}, \Delta\omega) \tag{1}$$

where P_c is the optical power circulating in the arm cavity, $\delta\nu_{hom}$ is the cavity linewidths (full width, half maximum) for the higher-order optical mode. The parameter Λ measures the spatial overlap between the acoustic and the higher-order optical modes; Γ is representative of the interferometer optical configuration and is a function of the 3-mode interaction tuning $\Delta\omega = \omega_m - 2\pi\Delta\nu_{hom}$, where $\Delta\nu_{hom}$ is the frequency difference between the fundamental and higher-order optical modes. For $\Delta\omega \to 0$, the parameter Γ reaches its maximum (see [15] for a more detailed description).

Unstable acoustic modes with parametric gain up to $R \simeq 100$ may arise in Advanced LIGO in the 10-90 kHz band [6]. To prevent these instabilities, a damping mechanism must be introduced to reduce the Q-factor of all unstable acoustic modes in this frequency band *without introducing excess thermal fluctuation in the detection band* of 10 Hz to 1 kHz.

III. MODEL OF THE ACOUSTIC MODE DAMPER (AMD)

In order to reduce the Q of test mass acoustic modes we designed a resonant AMD which can be attached to the test mass and provide dissipation via the piezo-electric effect.

In this section we first describe the interaction between the AMD and the test mass with a simple 1-D model, then we present a complete Finite Element Model of the entire system.

A. Simplified 1-D Model

The AMD and test-mass system can be described as a pair of coupled oscillators with a large mass ratio. The AMD mass m is attached to the much more massive test mass via piezo electric shear plates, which are modeled as a lossy spring with complex spring constant of magnitude k and loss angle η.

The test mass acoustic mode for which we would like to estimate the impact of the AMD is simplified in this model to a mass M, equal to the modal mass of the acoustic mode, attached to a fixed reference by a lossless spring K. The coupled systems is then excited by the radiation pressure force F applied to the TM mode, as shown in figure 2.

At frequencies near the resonance of the AMD, the lossy spring produced by the piezoelectric material and resistive load will dissipate the energy of the excited acoustic mode, as seen in figure 3.

For this system of coupled oscillators, the amplitude $A(\omega)$ of the acoustic mode driven by force F at angular frequency ω is

$$A(\omega) = \frac{F}{M\omega^2}\sqrt{\frac{\epsilon^2+\eta^2}{(\delta\epsilon+\mu)^2+\eta^2(\delta+\mu)^2}} \tag{2}$$

$$\text{where} \quad \delta = 1-\omega_0^2/\omega^2, \ \epsilon = 1-\omega^2/\omega_D^2$$
$$\omega_0^2 = \frac{K}{M}, \ \omega_D^2 = \frac{k}{m}, \ \text{and} \ \mu = \frac{m}{M}. \tag{3}$$

The resulting effective Q-factor is

$$Q_{\text{eff}} = \frac{\max(A(\omega))}{A(\omega=0)} \simeq \frac{\eta^2+(1-\rho)^2}{\eta\mu\rho} \tag{4}$$

where $\rho = \omega_0/\omega_D$, and we assume $\mu \ll 1$.

When the acoustic mode resonance is near that of the AMD, $\eta \gg |1-\rho|$, the acoustic mode Q is reduced to $Q_{\text{eff}} \simeq \eta/\mu$. When the acoustic mode resonance is well above the AMD resonance, $Q_{\text{eff}} \simeq \rho/\eta\mu$, and when it is well below the AMD resonance, $Q_{\text{eff}} \simeq 1/\eta\mu\rho$, assuming $\eta^2 \ll 1$.

To suppress PIs, the test mass acoustic mode Q-factors only need to be reduced from $\approx 10^7$ to $10^5 - 10^6$. Using

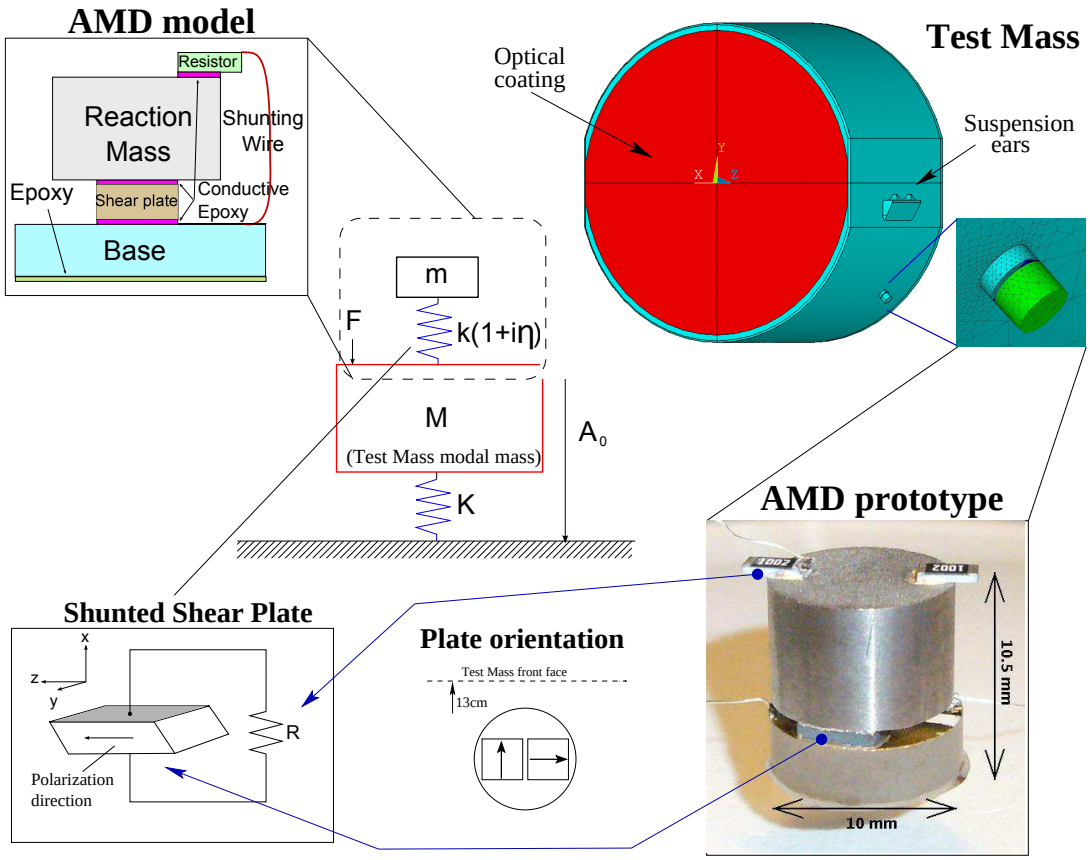

FIG. 2. Overview of the Acoustic Mode Damper (AMD). The AMD can be described as a small spring-mass system attached to a larger mass M. M represents a modal mass of an acoustic test mass mode which vibrates due to an external force F (radiation pressure). Such induced vibration causes deformation of the lossy spring of the damper. The non-zero loss angle of the damping spring (piezoelectric material) results in the lag of strain with respect to stress and thus energy dissipation. As a consequence of this dissipation process the amplitude of the acoustic mode vibration is reduced.

this simple model we can estimate that a 3g AMD with $\eta = 0.1$ on a 10kg test mass, can give $Q_{\rm eff} \lesssim 10^5$ for resonances with $\frac{1}{3} < \rho < 3$.

However, this model ignores a number of important factors. One of these is the location of the AMD relative to the nodes and anti-nodes of each test mass acoustic mode. Quantitatively speaking, the modal mass M of a given mode should be increased in this model by the ratio of the displacement at the AMD location to that of the mode's anti-node squared $M' = M(x_{\rm max}/x_{\rm AMD})^2$. Thus, an AMD located near a node will have a reduced value of μ, and will provide little damping.

Other important factors include the multiple coupled degrees of freedom of the AMD and the directional nature of the piezo damping material, both of which are covered in the follow section.

B. Finite Element Model (FEM)

The simple 1-D model introduced in the previous section is useful to provide an intuitive understanding of the AMD damping mechanism. However, it is inadequate to represent the details of the interaction between the AMD and the test mass acoustic modes (TMAMs). Each AMD has at least six resonant modes and hundreds of TMAMs are present in the frequency band of interest; a Finite Element Model is required in order to properly reproduce these modes and calculate the frequency overlap between them.

A FEM of the Advanced LIGO test mass with two attached AMDs was constructed with the ANSYS program [17]. The AMD model corresponds to the parameters of our prototype AMD (see table I), and the test mass model parameters are reported in table VI. All dissipation mechanisms in the test mass substrate, coating and bonds were included in the FEM, along with all the losses related to the acoustic mode damper structure (see table V for a full list).

A piezoelectric material (PZT), for which energy dissipation can be easily controlled, is ideal for AMD construction. The AMD design modeled here has 2 PZTs sandwiched between a reaction mass and the interferometer test mass (see figure 2). The PZTs respond to shear

TABLE I. List of the components for acoustic mode damper prototype. The dimensions and loss angle value are used in finite element modeling described in Sec. III B

Component	Material	Dimensions	Loss angle
Resistor	Ceramic, surface mount	0.7×1.2×0.5 mm^3	10 kΩ
Reaction mass	Tungsten	h=6.5 mm, d=9.6 mm	4e-5[a]
Epoxy	conductive TruDuct 2902	25 μm	0.15[a]
Piezo	shear plate TRS 200HD	4×4×0.76 mm^3	0.014
Base	fused silica + gold coating	h=3 mm, d=10 mm	$7.6 \cdot 10^{-12} \cdot f^{0.77}$[b]
Epoxy	non-conductive (EP30, MasterBond)	25 μm	0.1 [a]

[a] Assumed loss value.
[b] Loss obtained from [16].

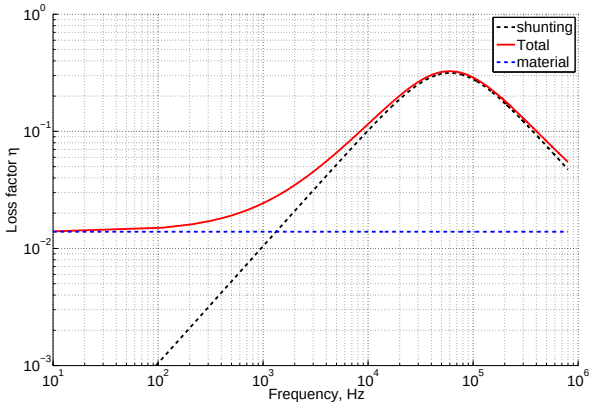

FIG. 3. A viscous-like behavior of the loss angle for shunted piezoelectric material. The total loss factor is a combination of the shunting loss and structural loss of the piezoelectric material. The maximum peak position is located at 40 kHz which corresponds to the shunt with 10 kΩ resistor. The larger the resistor the lower is frequency of the peak loss. The peak height is proportional to electromechanical coupling coefficient k_{15}. Note, the loss angle at low frequency section is mainly dominated by the structural loss angle of piezoelectric material.

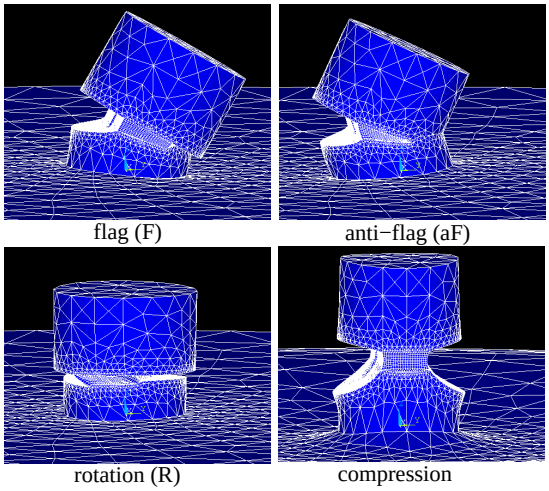

FIG. 4. Principal modes of AMD. The flag and anti-flag modes are in dublets due to AMD geometry. The difference between flag and anti-flag modes corresponds to the location of the rotation axis about which reaction mass rocks. For the flag pole the rotation axis is at the bottom surface of the shear plate whereas for the anti-flag mode the rotation axis is at the height of mass center of the reaction mass.

stress, and are poled orthogonally to ensure that all but 1 of the 6 lowest frequency AMD modes are damped. See figure 4 for mode shapes; the compression mode is not damped by the shear plates.

For the shear resonant damper, the spring constant can be associated with the shear deformation of the piezomaterial

$$k(1+i\eta) = Re(c_{55}^{su})\left(1+i\eta^{pzt}\right)\frac{S}{h}, \tag{5}$$

where c_{55}^{su} is the active shunted shear stiffness matrix component, S is the area, and h is the height of the shear plate, respectively.
The loss factor η^{pzt} is induced by shunting the shear plate with a resistor resulting in c_{55} becomes a complex quantity with a nonzero imaginary stiffness. The magnitude of $Im(c_{55})$ is strictly related to the impedance of the shear plate-resistor circuit. Thus, the loss factor of the shunted shear plate can be defined as

$$\eta^{pzt} = \frac{Im(c_{55}^{su})}{Re(c_{55}^{su})}. \tag{6}$$

Because the impedance of any PZT is capacitive, the loss factor η^{pzt} is frequency dependent. As such, careful selection of the shunting resistor and PZT dimensions can be used to maximize loss in the band of interest, as shown in figure 3. A more detailed discussion of the piezoelectric loss angle can be found in Appendix A.

We validated the FEM of the AMD by computing its principal resonances, and comparing them with direct measurements performed on a prototype AMD. The principal resonances were measured with a capacitive bridge circuit where one of the matching capacitors was the

TABLE II. Verification of the finite element model for AMD. Five principle resonances (two flag, two anti-flag and one rotational mode) obtained with the model are compared to the measured values. The x, y suffix corresponds to the shear plate orientation.

Mode type	FEM [kHz]	Measured [kHz]
Fy-mode	9.96	9.77
Fx-mode	12.87	12.61
R-mode	23.28	24.13
aFy-mode	38.36	37.39
aFx-mode	50.51	48.86

AMD prototype. A total of five principal resonances were identified, with three types of modes: two flag, two anti-flag, and one rotation mode (see table II). All these modes are characterized by large shear deformation for the double piezo configuration in the AMD. The sixth compression mode was not measured as it does not involve shear of the piezo plate. table II shows the good agreement between the output of the model and measurements on the AMD prototype.

Harmonic analysis (finite element analysis with an excitation at a fixed frequency) was conducted to estimate the Q-factor of each of the TMAMs. This approach allows us to include frequency dependent variables such as the shear plate stiffness $Re(c_{55}^{su})$, and its loss angle (see Appendix A).

The modal Q-factor of each resonant mode of the system was calculated as

$$Q(f_n) = \frac{\sum_m E_m(f_n)}{\sum_m E_m(f_n)\, tan(\phi_m)}, \tag{7}$$

where f_n is the frequency of the n^{th} acoustic mode (see figure 5). The loss associated with each structural component is treated separately; E_m is the strain energy stored in the m^{th} component and $\tan(\phi_m)$ is its loss factor (see tables I and VI).

The modeled resonant frequencies of 12 TMAMs were then compared to the measured resonance frequencies (see table III), obtained according to methods described in section IV. The front face displacement of the modes are shown in figure 5.

Note that the agreement between calculated and measured Q-values increases with frequency. According to the model, surface strain energy decreases with resonant frequency. This may indicate an additional dissipation process which is missing in the model. Nevertheless, a small relative frequency offset Δf below 1% in table III indicates a good agreement of the FEM with measured values.

TABLE III. The Q-factor of the test mass modes without AMDs installed. The 4th and 7th column correspond to the relative frequency noise Δf% and Q-factor ratio between calculated and measured value, respectively. Mode number corresponds to the first twelve modes with an anti-node in the center (drumhead modes).

Mode #	Freq. [Hz]	Freq. [Hz]	Δf %	Q-factor		
	FEM	Measured		FEM	Measured	Ratio
1	8128.3	8150.9	0.3	37M	1.9M	19.5
2	10391.1	10418.1	0.3	63M	14M	4.5
3	12999.1	12984.7	0.1	29M	15M	1.9
4	15101.4	15047.2	0.4	56M	17M	3.3
5	15151.0	15539.1	2.5	55M	16M	3.4
6	19487.0	19544.9	0.3	30M	7.0M	4.3
7	20113.6	20185.5	0.3	27M	13M	2.1
8	24824.0	24901.8	0.3	32M	16M	2.0
9	26504.3	26681.2	0.7	48M	18M	2.7
10	29767.4	29699.5	1.0	18M	15M	1.1
11	30912.1	31003.3	0.3	18M	12M	1.5
12	32664.1	32743.2	0.2	14M	13M	1.1

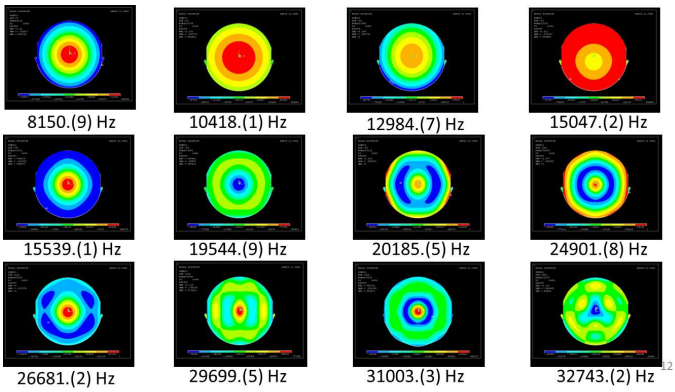

FIG. 5. Test mass drumhead modes for which Q-factor was measured. The color-code corresponds to the test mass front-face displacement amplitude. This figure was obtained from FEM analysis of the test mass model without AMDs.

IV. EXPERIMENTAL RESULTS

Several AMD prototypes were constructed, each consisting of six components (see table I):

Reaction Mass: A 10 g tungsten cylinder which tunes the AMD principal resonances to frequencies above 10 kHz is located on top of the shear plates.

Shear Plate: Two piezoelectric shear plates, oriented with perpendicular polarizations are glued to the reaction mass and base with conductive epoxy Tra-Duct2902. The epoxy serves to electrically connect the PZT electrodes to the reaction mass and base.

Base: The interface between flat shear plates and curved barrel of the test mass. The top flat surface is

gold coated with separate sections to which shear plates are glued. The bottom surface is curved to match the test mass barrel curvature. The base is made from fused silica and glued to the test mass with nonconductive epoxy.

Shunting circuit: One 10 kΩ resistor for each shear plate is glued to the reaction mass with conductive epoxy. The circuit is closed with 100 μm diameter silver coated copper wire, which is soldered to the resistor and gold coated surface of the base.

To measure Q-factors of the test mass modes, both with and without AMDs attached, a 16 m optical cavity was used, with the test mass forming the end mirror of the cavity. The test mass was suspended with monolithic fused silica suspension [18]. The optical cavity supports a 2 mm diameter Gaussian mode; the resonant beam probes the motion in the center of the test mass face, so that modes with an anti-node in the center of the mass are easily measured. A total of 12 modes were identified (figure 5) and measured, with the results shown in table III.

In order to measure the impact of the AMD on the Q of the TMAMs, several modes of the test mass were excited using electrostatic actuators [19] and their ring-down times observed. This measurement was repeated in three configurations: with no AMD, with 2 AMDs, with 2 AMDs which lacked resistive damping (shunt wires cut).

Each acoustic mode was detected in the cavity locking error signal as a peak in the Fourier domain. After being excited, each mode amplitude was recorded as a function of time to estimate the decay time τ. The Q-factor was determined from the decay time τ, according to

$$Q = \pi f_0 \tau. \tag{8}$$

where f_0 is the resonant frequency in Hz and τ is the exponential decay time constant.

Measurements of the test mass mode Q-factor performed after installing two AMDs clearly show the substantial damping capability of the AMD prototype, as reported in table IV (see also table VII in Appendix for additional details).

The results indicate that out of 12 modes, 11 are suppressed by at least factor of 10 and in some cases by more than two orders of magnitude. The relatively large discrepancy between model and measurement for mode #2 can be explained by the AMD and test mass (TM) interaction condition for this particular mode. The FEM predicts that mode #2 will be within 500Hz of the AMD Fy-mode at 10 kHz, while the measured values give a separation of 800Hz (mostly due to the AMD resonance being off), reducing the interaction between the AMD and TM mode.

In the off-resonance interactions, which are more common and set the lower limit to AMD performance, the discrepancy is generally less than a factor of a few.

Surprisingly, modes #2 and #6 show a counterintuitive behavior; opening the resistive circuit of the AMDs decreases the TMAM Q-factor. However, since the electrical circuit of AMD affects the mechanical stiffness of the shear plates, it is expected that the principal resonances also changed when the circuit is opened. And, if the AMD resonance is close to the TMAM frequency, equation 4 indicates that the mode Q can be decreased by *lowering* the AMD loss.

The large Q reduction for modes #3 and #4 is due to the on-resonance interaction between TMAM and AMD, whereas for modes #5 and #12 the large Q reduction is due to the anti-node AMD location on the TMAM.

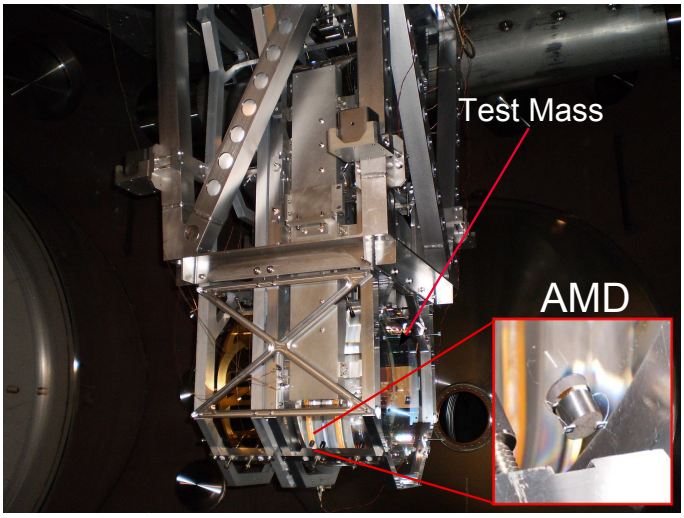

FIG. 6. Two acoustic mode dampers attached to the barrel of a suspended aLIGO-like test mass. The AMDs are on opposite sides of the test mass, $\sim 45^\circ$ down from the midline.

TABLE IV. Test mass mode suppression obtained with two AMDs. The damping factor refers two overall mode damping efficiency where the resistive contribution corresponds to the contribution of the shunt to the damping mechanism.

Mode #	Freq. [Hz]	Damping factor	Resistive contribution [%]
1	8150.9	32.2	12
2	10418.1	31.8	-57
3	12984.7	441.2	21
4	15047.2	81.0	9
5	15539.1	>320	>71
6	19544.9	15.6	-2
7	20185.5	13.8	41
8	24901.8	5.2	4
9	26681.2	>360	>0
10	29699.5	23.8	43
11	31003.3	307.7	68
12	32743.2	>260	>4

V. ANALYSIS OF THE AMD THERMAL NOISE

The AMD is designed to increase the mechanical damping of the test mass acoustic modes above 10 kHz. At the same time, the AMD must introduce minimal additional mechanical loss in the 10-1000 Hz band, where low mechanical loss is required to keep test mass thermal noise small [20]. Thus it is critical to calculate the thermal noise resulting from the AMDs in our overall evaluation of this PI mitigation technique.

We used the FEM described above to calculate the thermal noise resulting from our experimental test of two AMDs attached to a test mass. The AMD thermal noise was calculated numerically at 100 Hz, the most sensitive part of the detection band, using Levin's approach [21]. The energy dissipation per cycle was computed using equation A15 for a pressure profile corresponding to the Advanced LIGO geometry (laser beam radius $\omega_0 = 5.5$ cm, incident on the front face of the TM). Results are shown in table V.

The test mass thermal noise level of $5.2 \times 10^{-21}\mathrm{m}/\sqrt{\mathrm{Hz}}$ corresponds to the design level for Advanced LIGO, and is dominated by optical coating loss [22, 23]. As table V shows, while our *prototype* AMD would contribute significantly to thermal noise, it is not orders of magnitude above the more fundamental sources of thermal noise.

TABLE V. Thermal noise budget for test mass and acoustic mode damper prototype when attached to the test mass. The thermal noise was calculated for the laser beam spot size of $\omega = 5.5$ cm.

Component	Thermal noise @ 100 Hz $[10^{-21} m/\sqrt{Hz}]$
Test Mass:	
Substrate	0.8
Optical coating	5.1
Suspension ears	0.0
Ears bond	0.6
Total per TM	**5.2**
AMD:	
Reaction mass (RM)	0.3
Epoxy (RM-PZT)	4.8
Shear plate (PZT-X)[a]	5.5
Shear plate (PZT-Y)[a]	5.5
Epoxy Base-PZT	7.2
Base	0.0
Epoxy Base-TM	6.0
Total per AMD	**13**

[a] A product of a structural+resistive loss angle. Note that a major contribution to that value comes from the structural loss, see figure 3.

Relative to the prototype device, our model points to several design and material improvements that can be made to significantly reduce the thermal noise impact. The major AMD thermal noise contributors are the epoxies used to bond the AMD elements, and structural loss in the piezo shear plates. The former can be improved with lower loss epoxy and thinner bond layers. The latter can be improved with a more suitable choice of piezo material.

Other design elements can also be altered. The mass of the reaction mass can be reduced to lower the thermal noise without significantly affecting the acoustic mode damping performance. Another modification would be to avoid alignment of the piezo shear plate polarization with the laser beam axis, to minimize the contribution of resistive loss to the thermal noise. These and other design optimizations will be explored in a future paper.

VI. CONCLUSION

Acoustic mode dampers represent a simple yet effective approach to damping parametric instabilities. The great advantage of this approach over active damping [10] is that many test mass acoustic modes are effected simultaneously, and no further intervention is necessary. This is likely to be a critical feature in instruments that would otherwise suffer from multiple acoustic modes simultaneously excited by parametric instabilities.

The investigation presented here involved modeling and construction of a prototype AMD, which was shown to effectively damp test mass acoustic modes. The thermal noise associated with this prototype AMD was also computed. Though the prototype AMD does not meet the stringent thermal noise requirements of gravitational wave detectors, several design elements were identified for improvement, making this approach a potentially viable solution to parametric instabilities.

ACKNOWLEDGMENTS

The authors gratefully acknowledge the support of the National Science Foundation and the LIGO Laboratory, operating under cooperative Agreement No. PHY-0757058 This paper has been assigned LIGO Document No. LIGO-P1400257.

[1] G. M. Harry and the LIGO Scientific Collaboration, Classical and Quantum Gravity **27**, 084006 (2010).
[2] J. Degallaix, T. Accadia, F. Acernese, M. Agathos, A. Allocca, P. Astone, G. Ballardin, F. Barone, M. Barsuglia, A. Basti, T. S. Bauer, M. Bebronne, M. Bejger, M. G. Beker, and M. Bitossi, "Advanced virgo status," (2013).
[3] K. Somiya, Classical and Quantum Gravity **29**, 124007 (2012).
[4] B. Sathyaprakash and F. Schutz, Living Rev. Relativity **12** (2009), 10.12942/lrr-2009-2.
[5] C. Zhao, L. Ju, Y. Fan, S. Gras, B. J. J. Slagmolen, H. Miao, P. Barriga, D. G. Blair, D. J. Hosken, A. F. Brooks, P. J. Veitch, D. Mudge, and J. Munch, Phys. Rev. A **78**, 023807 (2008).
[6] M. Evans, L. Barsotti, and P. Fritschel, Physics Letters A **374**, 665 (2010).
[7] S. Gras, C. Zhao, D. G. Blair, and L. Ju, Classical and Quantum Gravity **27**, 205019 (2010).
[8] C. Zhao, L. Ju, J. Degallaix, S. Gras, and D. G. Blair, Phys. Rev. Lett. **94**, 121102 (2005).
[9] Z. Zhang, C. Zhao, L. Ju, and D. G. Blair, Phys. Rev. A **81**, 013822 (2010).
[10] J. Miller, M. Evans, L. Barsotti, P. Fritschel, M. MacInnis, R. Mittleman, B. Shapiro, J. Soto, and C. Torrie, Physics Letters A **375**, 788 (2011).
[11] S. Gras, D. G. Blair, and C. Zhao, Classical and Quantum Gravity **26**, 135012 (2009).
[12] V. Braginsky, S. Strigin, and S. Vyatchanin, Physics Letters A **287**, 331 (2001).
[13] L. Ju, S. Gras, C. Zhao, J. Degallaix, and D. Blair, Physics Letters A **354**, 360 (2006).
[14] X. Chen, C. Zhao, L. Ju, S. Danilishin, D. Blair, H. Wang, and S. P. Vyatchanin, Arxiv preprint hep-th (2013).
[15] S. Strigin and S. Vyatchanin, Physics Letters A **365**, 10 (2007).
[16] S. D. Penn, A. Ageev, D. Busby, G. M. Harry, A. M. Gretarsson, K. Numata, and P. Willems, Physics Letters A **352**, 3 (2006).
[17] "Ansys academic research, release 14.0,".
[18] A. V. Cumming, A. S. Bell, L. Barsotti, M. A. Barton, G. Cagnoli, D. Cook, L. Cunningham, M. Evans, G. D. Hammond, G. M. Harry, A. Heptonstall, J. Hough, R. Jones, R. Kumar, R. Mittleman, N. A. Robertson, S. Rowan, B. Shapiro, K. A. Strain, K. Tokmakov, C. Torrie, and A. A. van Veggel, Classical and Quantum Gravity **29**, 035003 (2012).
[19] L. Carbone, S. M. Aston, R. M. Cutler, A. Freise, J. Greenhalgh, J. Heefner, D. Hoyland, N. A. Lockerbie, D. Lodhia, N. A. Robertson, C. C. Speake, K. A. Strain, and A. Vecchio, Classical and Quantum Gravity **29**, 115005 (2012).
[20] H. Callen and R. Greene, Phys. Rev. **86**, 702 (1952).
[21] Y. Levin, Phys. Rev. D **57**, 659 (1998).
[22] G. M. Harry, A. M. Gretarsson, P. R. Saulson, S. E. Kittelberger, S. D. Penn, W. J. Startin, S. Rowan, M. M. Fejer, D. R. M. Crooks, G. Cagnoli, J. Hough, and N. Nakagawa, Classical and Quantum Gravity **19**, 897 (2002).
[23] M. Evans, S. Ballmer, M. Fejer, P. Fritschel, G. Harry, and G. Ogin, Physical Review D **78** (2008).
[24] N. Hagood and A. von Flotow, Journal of Sound and Vibration **146**, 243 (1991).
[25] ANSI/IEEE Std 176-1987 (1988), 10.1109/IEEESTD.1988.79638.
[26] The information about the imaginary part of the stiffness matrix is not available. We assumed that the material loss factor corresponds to the Q-factor of the piezomatrial provided by the manufacturer. In our opinion low Q PZT should have fairly constant loss for all stiffness components.
[27] G. M. Harry *et al.*, Classical and Quantum Gravity **24**, 405 (2007).

Appendix A: Piezoelectric material

Any piezoelectric material is strictly characterized by electromechanical properties. The fact that both electrical and mechanical properties are inseparable allows us to represent the dissipation process in a shunted piezoelectric material either as a Johnson heat or mechanical loss. For the purpose of this work we focus on disspation process in terms of the mechanical loss.
From the stress-charge of the piezoelectric constitutive

equation it is straightforward to derive the total induced stress in the shunted piezoelectric material [24]. Assuming no external current plugged to the piezoelement electrode we get

$$\boldsymbol{\sigma}_{(6\times1)} = \left(\boldsymbol{c}^{E}_{(6\times6)} - i\omega \boldsymbol{e}^{t}_{(6\times3)} \boldsymbol{Z}^{TOT}_{(3\times3)} \boldsymbol{A}_{(3\times3)} \boldsymbol{e}_{(3\times6)} \boldsymbol{L}^{-1}_{(3\times3)}\right) \boldsymbol{S}_{(6\times1)}, \tag{A1}$$

where $\boldsymbol{c}^E$ is the mechanical stiffness matrix under constant electric field, $\boldsymbol{e}^t$ and $\boldsymbol{e}$ are the piezoelectric stress constant. The upper script t refers to transpose operator [25]. Electrode area is represented by matrix $\boldsymbol{A}$, whereas thickness of the piezomaterial between electrodes by matrix $\boldsymbol{L}$. The strain $\boldsymbol{S}$ is a product of the acting stress $\boldsymbol{\sigma}$ on piezo-element and charge accumulation in the piezoelement. Each bracket corresponds to the matrix dimenssion. It is assumed that piezoelectric element has a brick shape thus matrices $\boldsymbol{Z}^{TOT}$,$\boldsymbol{A}$, and $\boldsymbol{L}$ are diagonal.
The total impedance in equation A1 is inverse sum of the piezoelement admittance under constant electric field $\boldsymbol{Y}^E$ and the admittance of the external circuit $\boldsymbol{Y}^{su}$ connected to the piezoelement electrodes, thus

$$\boldsymbol{Z^{TOT}} = \left(\boldsymbol{Y}^{E} + \boldsymbol{Y}^{su}\right)^{-1}. \tag{A2}$$

The admittance of piezelement $\boldsymbol{Y}^E$ is assumed to be exclusively capacitive. Hence,

$$\boldsymbol{Y}^{E} = i\omega \boldsymbol{A}\boldsymbol{\epsilon}^{S}\boldsymbol{L}^{-1} = i\omega \boldsymbol{C}^{S} = i\omega \boldsymbol{C}^{T}\left(\boldsymbol{\epsilon}^{T}\right)^{-1}\boldsymbol{\epsilon}^{S}, \tag{A3}$$

where $\boldsymbol{C}$, $\boldsymbol{\epsilon}$ is the capacitance and the dielectric constant matrices under constant strain S and constant stress T, respectively. It is convenient to operate with $\boldsymbol{C}^T$ since this quantity can be easily measured at stress free conditions and no shortened piezelement electrodes.
According to equation A1, if the piezoelement is integrated with a nonzero impedance electric circuit, the imaginary part of the stiffness tensor arises. The imaginary part can be interpreted as a dissipative component of the stiffness tensor. The total shunted stiffness matrix is

$$\boldsymbol{c}^{su} = \boldsymbol{c}^{E} - i\omega \boldsymbol{e}^{t}\boldsymbol{Z}^{TOT}\boldsymbol{A}\boldsymbol{e}\boldsymbol{L}^{-1}. \tag{A4}$$

Because matrices $\boldsymbol{A}$, $\boldsymbol{Z}^{TOT}$, and $\boldsymbol{L}$ are diagonal and knowing that $\boldsymbol{A}\boldsymbol{L}^{-1} = \boldsymbol{C}^{T}(\boldsymbol{\epsilon}^{T})^{-1}$ equation A4 can be written as

$$\boldsymbol{c}^{su} = \boldsymbol{c}^{E} - \boldsymbol{e}^{t}\boldsymbol{e}\widehat{\boldsymbol{Z}}\left(\boldsymbol{\epsilon}^{S}\right)^{-1}, \tag{A5}$$

where $\widehat{\boldsymbol{Z}}$ is the nondemensional impedance

$$\widehat{\boldsymbol{Z}} = \boldsymbol{Z}^{TOT}\boldsymbol{Y}^{E}. \tag{A6}$$

Note, for zero impedance the shunted circuit sets $\widehat{\boldsymbol{Z}}$ to be a unity matrix $\widehat{\boldsymbol{Z}} = \boldsymbol{I}$ whereas for the nonzero impedance shunting $\widehat{\boldsymbol{Z}}$ is a complex quantity. Using indexing equation A4 can be written as

$$c^{su}_{ij} = c^{E}_{ij} - \frac{e_{ki}e_{kj}\widehat{Z}_{kk}}{\epsilon^{S}_{kk}}. \tag{A7}$$

where $k = 1, 2, 3$ and corresponds to the electrode position, $\boldsymbol{\epsilon}^S$ is the dielectric permittivity of the piezoelectric material. It is a general equation for the stiffness matrix of PZT with arbitrary number of electrode pairs.

From equation A3 and A7 becomes clear that loss can be controlled with the shunting circuit. Moreover, such loss is in fact a frequency dependent quantity with loss curve shape dependent on shunting circuit.

For the shear plate with the single pair of electrodes, which is our case, only a stiffness matrix element c^{su}_{55} is affected by shunting resistor, thus

$$c^{su}_{55} = c^{E}_{55} - \frac{e_{15}e_{15}\widehat{Z}_{11}}{\epsilon^{S}_{11}}. \tag{A8}$$

and the nondemensional complex impedance $\widehat{Z}_{kk}$ has a single nonunity element

$$\widehat{Z}_{11} = \frac{i\omega\epsilon^{S}_{11}RC^{T}}{i\omega\epsilon^{S}_{11}RC^{T} + \epsilon^{T}_{11}} = \frac{\left(\omega\epsilon^{S}_{11}RC^{T}\right)^{2}}{\left(\omega\epsilon^{S}_{11}RC^{T}\right)^{2} + \left(\epsilon^{T}_{11}\right)^{2}} + i\frac{\omega\epsilon^{S}_{11}\epsilon^{T}_{11}RC^{T}}{\left(\omega\epsilon^{S}_{11}RC^{T}\right)^{2} + \left(\epsilon^{T}_{11}\right)^{2}}. \tag{A9}$$

Since the stiffness matrix $\boldsymbol{c}^{su}$ is a complex quantity we can define the loss factor $\boldsymbol{\eta}$ as

$$\boldsymbol{\eta} = \frac{Im(\boldsymbol{c}^{su})}{Re(\boldsymbol{c}^{su})}, \tag{A10}$$

and thus

$$\eta_{ij} = \frac{Im(\widehat{Z}_{kk})\chi_{kij}}{Re(\widehat{Z}_{kk})\chi_{kij} + 1}, \tag{A11}$$

where $\chi_{kij} = e_{ki}e_{kj}(c^{E}_{ij}\epsilon^{S}_{kk})^{-1}$. Index k is associated with the electrodes orientation, whereas indices i and j correspond to stress-strain directions in the stiffness matrix $\boldsymbol{c}^{su}$. The shunting loss factor of the shear plate becomes

$$\eta_{55} = \frac{Im(\widehat{Z}_{11})\chi_{155}}{Re(\widehat{Z}_{11})\chi_{155} + 1}. \tag{A12}$$

This is the main loss mechanism based on which shear AMDs operate. The quantity χ_{155} is simply a function of electromechanical coupling coefficient k_{15} and is equal

to $\chi_{155} = \frac{k_{15}^2}{1-k_{15}^2}$. Note, that according to equation A8, the material stiffness (the real part of c_{55}^{su}) is also reduced and should be included in the analysis.

1. Total mechanical loss angle

An assumption of the stiffness matrix being real in the absence of shunt is not sufficient for accurate estimation of energy dissipation. It becomes especially important in the thermal noise analyisis, see Sec. V.
For known material loss angle of the nonshunted piezoelement, the total loss factor of the piezoelectric material can be defined as

$$\eta_{ij}^{tot} = \frac{tan(\phi_{ij}^{mat}) + Im(\widehat{Z}_{kk})\chi_{kij}}{1 + Re(\widehat{Z}_{kk})\chi_{kij}}, \tag{A13}$$

where $\tan(\phi_{ij}^{mat})$ is the material loss factor matrix of piezo-element. The loss factor $\tan(\phi_{ij}^{mat})$ of $\boldsymbol{c^E}$ can be easily computed using equation A10.

All piezoelectric material has anisotropic structure which implies that strain energy dissipation in such material must depend on the piezoelement geometric shape. It is more convenient to use effective loss angle ϕ_{eff} rather than the loss angle ϕ for each stiffness matrix component. We define the energy dissipation per cycle in the piezo-element

$$W_{dis} = 2\pi W_{st}\eta_{eff} \tag{A14}$$

$$= 2\pi \int Re(S_i S_j^*) Re(c_{ji}^{su})\eta_{ji}^{tot} dV \tag{A15}$$

where W_{st} is the stored strain energy such that $2\pi W_{st} = \int Re(S_i T_j^*) dV$, where S, T are the complex strain and stress, respectively and V is the volume of the piezo-element.
Since the loss factor of the piezoelement is inverse of its Q-factor or equally a ratio of dissipated energy per cycle W_{dis} to energy stored W_{st} in the piezoelement, we can define the effective noise fuctor η_{eff}

$$\eta_{eff} = \frac{W_{dis}}{2\pi W_{st}} = \frac{\int Re(S_i S_j^*) Re(c_{ji}^{su})\eta_{ji}^{tot} dV}{\int Re(S_i T_j^*) dV}, \tag{A16}$$

where S, T are the complex strain and stress, respectively and V is the volume of the piezo-element. This is a key equation in the finite element analysis which properly estimates the contribution of piezoelement in the strain energy dissipation in the test mass.

In our analysis we assumed constant material intrinsic loss factor for all $\boldsymbol{c}^E$ elements equal to $\tan(\phi_{ij}^{mat})$=0.014 [26], which leads to

$$\eta_{55}^{tot} = \frac{0.014 + Im(\widehat{Z}_{11})\chi_{155}}{1 + Re(\widehat{Z}_{11})\chi_{155}}. \tag{A17}$$

Note, the remaining elements of the shunting induced loss η_{kij}^{tot} are equal to the material structural loss factor. The total loss angle for the c_{55}^E stiffness element is shown in figure 3.

Appendix B: Additional Tables

TABLE VI. Values for the aLIGO end test mass parameters used in this paper.

Optical parameters:			
End test mass transmissivity	5.0 ppm		
1 layer each of Ta_2O_5/SiO_2 with thickness of 2.32 μm, and 3.49 μm[a], respectively			
Mechanical properties of optical coating and ear bond:			
	Ta_2O_5	SiO_2	Ear bond
Young's modulus	140 GPa	70 GPa	7.2 GPa
Poisson ratio	0.23	0.17	0.17
Density	8300 kg/m^3	2201 kg/m^3	2202 kg/m^3
Refractive index	2.06539	1.45	-
Loss angle[b]	$2.4{\cdot}10^{-4}$+f$\cdot 1.8{\cdot}10^{-9}$	$0.4{\cdot}10^{-4}$+f$\cdot 1.1{\cdot}10^{-9}$	0.1
Test mass dimensions:			
Radius	0.17 m		
Thickness	0.2 m		
Flats width	0.095 m		
Wedge angle	0.07 deg		
Mass	40 kg		
Loss angle[c]	$7.6{\cdot}10^{-12}$.f $^{0.77}$		
Material[c]	fused silica		

[a] For the purpose of numerical analysis, a multilayer coating was reduced to double layers with a total thickness which corresponds to the sum of all 18/19 layers of Ta_2O_5/SiO_2 for the ETM.
[b] f-frequency. Note, the difference in loss angles for the substrate, and for the optical coating made from fused silica. Losses were obtained from [27]. Additionally, coating loss angles were revised to the current measured values.
[c] Both test mass and suspension ears.

TABLE VII. Results of the Q-factor measurement with attached AMDs for shunted and non-shunted cases.

	Q-factor			
Mode #	Resistive		Open Circuit	
	FEM	Measured	FEM	Measured
1	52k	59k	70k	67k
2	7.9k	440k	9.9k	280k
3	23k	34k	23k	43k
4	420k	210k	510k	230k
5	2.4M	<50k	2.2M	170k
6	1.9M	450k	4.8M	440k
7	1.1M	940k	1.6M	1.6M
8	6.7M	3.1M	9.5M	3.2M
9	49k	<50k	64k	<50k
10	1.9M	630k	3.3M	1.1M
11	61k	39k	116k	120k
12	25k	<50k	260k	52k